Infrared Nanospectroscopy Reveals the Chemical Nature of Pit Membranes in Water-Conducting Cells of the Plant Xylem[1]

Luciano Pereira,[a,2] Denisele N.A. Flores-Borges,[a,2] Paulo R.L. Bittencourt,[a,2] Juliana L.S. Mayer,[a,2] Eduardo Kiyota,[a] Pedro Araújo,[a] Steven Jansen,[b] Raul O. Freitas,[c] Rafael S. Oliveira,[a] and Paulo Mazzafera[a,d,3]

[a]Department of Plant Biology, Institute of Biology, University of Campinas, 13083-970 Campinas, Sao Paulo, Brazil
[b]Ulm University, Institute of Systematic Botany and Ecology, 89081 Ulm, Germany
[c]Brazilian Synchrotron Light Laboratory, Brazilian Center for Research in Energy and Materials, 13083-970 Campinas, Sao Paulo, Brazil
[d]Department of Crop Production, School of Agriculture Luiz de Queiroz, University of São Paulo, 13418-900 Piracicaba, Sao Paulo, Brazil

ORCID IDs: 0000-0003-2225-2957 (L.P.); 0000-0002-8500-3205 (D.N.F.); 0000-0002-1618-9077 (P.R.B.); 0000-0001-7439-5234 (J.L.M.); 0000-0001-6322-3461 (E.K.); 0000-0002-3205-5749 (P.A.); 0000-0002-4476-5334 (S.J.); 0000-0002-3285-5447 (R.O.F.); 0000-0002-6392-2526 (R.S.O.); 0000-0001-9073-4056 (P.M.)

In the xylem of angiosperm plants, microscopic pits through the secondary cell walls connect the water-conducting vessels. Cellulosic meshes originated from primary walls, and middle lamella between adjacent vessels, called the pit membrane, separates one conduit from another. The intricate structure of the nano-sized pores in pit membranes enables the passage of water under negative pressure without hydraulic failure due to obstruction by gas bubbles (i.e. embolism) under normal conditions or mild drought stress. Since the chemical composition of pit membranes affects embolism formation and bubble behavior, we directly measured pit membrane composition in *Populus nigra* wood. Here, we characterized the chemical composition of cell wall structures by synchrotron infrared nanospectroscopy and atomic force microscopy-infrared nanospectroscopy with high spatial resolution. Characteristic peaks of cellulose, phenolic compounds, and proteins were found in the intervessel pit membranes of *P. nigra* wood. In addition, the vessel to parenchyma pit membranes and developing cell walls of the vascular cambium showed clear signals of cellulose, proteins, and pectin. We did not find a distinct peak of lignin and other compounds in these structures. Our investigation of the complex chemical composition of intervessel pit membranes furthers our understanding of the flow of water and bubbles between neighboring conduits. The advances presented here pave the way for further label-free studies related to the nanochemistry of plant cell components.

Intervessel pit membranes, which represent porous media developed from a modified primary cell wall and the middle lamella between two neighboring vessels, play an essential role in regulating the long-distance transport of sap through the xylem tissue of plants. The nanoscale pores of pit membranes account for approximately 50% of the hydraulic resistivity of water transported through dead xylem conduits (Sperry et al., 2006). Pit membranes seem to function as safety valves, preventing hydraulic failure caused by gas entry and the spreading of vascular pathogens. However, plant transpiration may generate strong negative pressure in xylem conduits, and air bubbles can force their way through the membrane nanopores, which may result in the spread of embolism. This process of air seeding occurs when an air bubble from an adjacent air space is sucked into a water-filled lumen via a pore in the pit membrane (Zimmermann, 1983). Although the mechanism behind air seeding remains poorly understood, it is clear that the pit membrane ultrastructure and chemical composition determine the likelihood of air seeding. Therefore, pit membranes are key structures in the plant water transport system, modulating both water transport efficiency and safety (Choat et al., 2008).

Water transport and embolism spreading via pit membranes occur through nano-sized pores, which are typically smaller than 50 nm in angiosperms, although both structural and chemical properties are determinants of air seeding. Both the efficiency and safety of water transport depend on geometrically complex pore volumes (Jansen et al., 2009; Li et al., 2016) and on

[1]L.P. thanks the São Paulo Research Foundation for the fellowship granted (FAPESP, grant no. 2017/14075-3). J.L.S.M., R.S.O., and P.M. thank the National Council for Scientific and Technological Development (CNPq, Brazil) for their fellowships.

[2]These authors contributed equally to the article.

[3]Address correspondence to pmazza@unicamp.br.

The author responsible for distribution of materials integral to the findings presented in this article in accordance with the policy described in the Instructions for Authors (www.plantphysiol.org) is: Paulo Mazzafera (pmazza@unicamp.br).

P.M. and L.P. conceived the research; P.M., L.P., D.N.A.F.-B., P.R.L.B., J.L.S.M., E.K., P.A., S.J., R.O.F., and R.S.O. planned and performed the experiments; P.M., S.J., R.O.F., and R.S.O. assisted substantially with writing the article.

www.plantphysiol.org/cgi/doi/10.1104/pp.18.00138

how hydrophilic or hydrophobic pit membranes are (McCully et al., 2014; Herbette et al., 2015; Jansen and Schenk, 2015; Schenk et al., 2015, 2017). Although there is convincing evidence for drought-induced embolism via air seeding, the actual mechanisms associated with air seeding are poorly understood. Pit membrane integrity, which is likely determined by its ultrastructural, mechanical, and chemical properties, plays an important role in the plant's resistance to embolism. The damage of pit membranes associated with shrinkage after embolism events may lead to increased vulnerability to embolism via air seeding fatigue (Hacke et al., 2001; Tixier et al., 2014; Hillabrand et al., 2016; Zhang et al., 2017). Thus, a precise understanding of the chemical composition of pit membranes is essential for answering questions and improving the discussion on how plants transport water under negative pressure (Jansen and Schenk, 2015; Schenk et al., 2017).

While there is general agreement that intervessel pit membranes are composed of cellulose fibers, it is less clear to what extent other compounds might be involved. Yet, direct assessments of their composition were based on low-spatial-resolution methods, such as ultraviolet microspectrophotometry (Bauch and Berndt, 1973; Sano and Fukuzawa, 1994; Schmitz et al., 2008) and x-ray spectromicroscopy (Boyce et al., 2004). Indirect methods employed electron microscopy based on staining techniques (Fineran, 1997; Fromm et al., 2003; Schenk et al., 2017) and immunocytochemistry (Sun et al., 2011, 2013, 2017; Kim and Daniel, 2013; Herbette et al., 2015; Klepsch et al., 2016). During cell apoptosis, hydrolytic enzymes have been suggested to remove noncellulosic polysaccharides such as hemicellulose and pectin (O'Brien, 1970; Kim and Daniel, 2013; Herbette et al., 2015; Klepsch et al., 2016), although there are contradictory results about noncellulosic compounds (Bamber, 1961; Sano and Fukuzawa, 1994; Fineran, 1997; Donaldson, 2001) such as lignin (Fromm et al., 2003; Boyce et al., 2004; Schmitz et al., 2008, 2012; Herbette et al., 2015). More recently, amphiphilic lipids were shown to be associated with intervessel pit membranes; these lipids could play a crucial role in the generation of surfactant-coated nanobubbles (Jansen and Schenk, 2015; Schenk et al., 2017, 2018). Considering the scale of the pit membrane, with a few hundred molecules comprising a 15- to 30-nm-thick cellulose microfibril and a general thickness of 200 to 1,000 nm in freshly embedded transmission electron microscopy samples, it is reasonable to assume that the aforementioned methods were not accurate enough to detect less abundant compounds.

Our incomplete understanding of the chemical composition of pit membranes is at least partly due to the nanoscopic dimensions of pit membrane microfibrils. Recent advances in infrared (IR) spectroscopy allow chemical analysis beyond the classical diffraction limit of light. Scattering scanning near-field optical microscopy (s-SNOM; Kawata and Inouye, 1995; Zenhausern et al., 1995; Knoll and Keilmann, 1999) and photothermal expansion spectral imaging and spectroscopy (atomic force microscopy infrared nanospectroscopy, orAFM-IR) are among the few techniques capable of studying the nanochemistry of materials. In s-SNOM, light is confined at the apex of an atomic force microscopy (AFM) tip that works as a nanoantenna for creating subdiffraction light confinement (nano-source). The spatial resolution is then no longer defined by the light wavelength but by the form factor of the antenna, typically a radius of ~25 nm (Keilmann and Hillenbrand, 2004). Hence, s-SNOM is suitable for the study of the optochemistry of organic (Huth et al., 2012; Amenabar et al., 2013; Govyadinov et al., 2013) and inorganic (Huber et al., 2009, 2010; Amarie et al., 2012) material at the nanoscale. When combined with synchrotron IR radiation, s-SNOM allows for broadband IR nanospectroscopy across the whole mid-IR range. In AFM-IR, the local volume expansion of a material induced by narrow-band laser illumination is mechanically monitored by AFM.

Here, we combine s-SNOM with ultra-broadband synchrotron infrared radiation (SINS; Fig. 1; Hermann et al., 2013; Bechtel et al., 2014; Pollard et al., 2016; Freitas et al., 2018) to assess the nanochemistry of pit membranes inside the IR fingerprint spectral region. Complementary to these SINS measurements, we present nanoscale resolved narrow-band chemical imaging by means of local molecular thermal expansion employing AFM-IR (Dazzi et al., 2005, 2006, 2010; Lu et al., 2014). Although sample preparation is a bottleneck for SINS, and some compounds may be degraded in dry conditions without fixative, as used here (Schenk et al., 2018), the combination of both techniques allowed us to qualitatively determine the nanochemistry of intervessel pit membranes, vessel-parenchyma pit membranes, and developing primary cell wall of *Populus nigra*.

RESULTS

SINS

A summary of all characteristic IR peaks using SINS is shown in Table 1, with reference to the cell wall compounds based on the literature. The spectra of all structures measured are shown in Supplemental Figure S1. Intervessel pit membranes showed characteristic IR peaks of cellulose (O-H and C-O-C vibrations at 1,205 and 1,145 cm^{-1}), cellulose or hemicellulose (1,315 cm^{-1}), and phenolic compounds (C=C vibrations at 1,625 and 1,510 cm^{-1}; Fig. 2A). The spectra also showed a weaker signal related to amide II (C=N and N-H vibrations at 1,550 cm^{-1}), which indicated the presence of proteins.

Vessel-to-parenchyma pit membranes and developing cell walls of the vascular cambium showed clear signals of cellulose (1,205 and 1,145 cm^{-1}), amides (1,550 and 1,460 cm^{-1}), and pectin (1,105 and 1,075 cm^{-1}; Fig. 2, B and C). A distinct lignin peak was not present in the vessel-to-parenchyma pit membrane at 1,510 cm^{-1}, and the 1,625 cm^{-1} peak cannot be separated from the

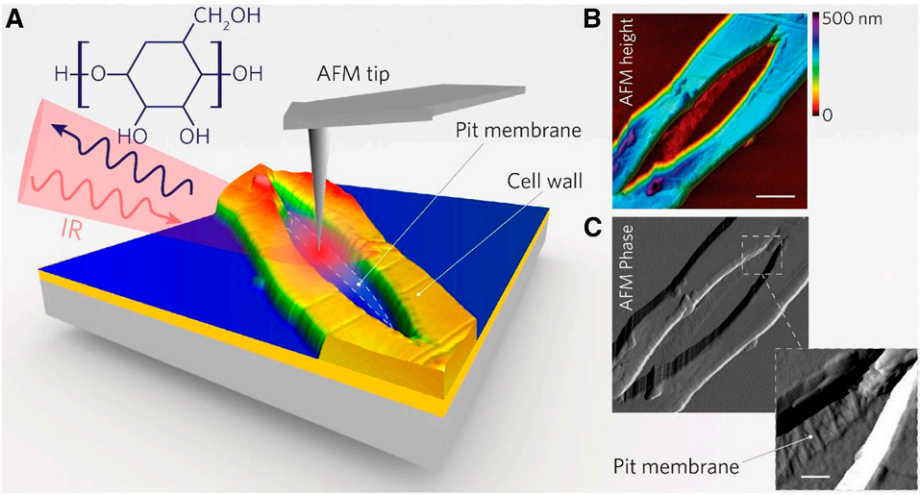

Figure 1. A, Scheme of SINS measurements of an intervessel pit membrane of *P. nigra*. The AFM tip acts as a broadband antenna for the IR radiation from the synchrotron, creating a subdiffractional IR probe. The tip-sample interaction inside an area of 25 × 25 nm produces a scattered signal that carries information of the IR absorption from the sample (IR absorbance), revealing the nanoscale chemistry of the material. B and C, AFM topography (B) and phase (C) were acquired simultaneously to the s-SNOM experiment. The inset in C reveals the pit membrane nanofibers arranged as a mesh. Bars = 1 µm (B) and 200 nm (inset in C).

1,640 cm^{-1} amide I peak characteristic of many compounds (Fig. 2). In the same way, developing cell walls show clear peaks of amides (1,550 and 1,460 cm^{-1}) but weaker signals of other compounds (Fig. 2C).

AFM-IR

Single-point spectra from all cell wall structures presented a strong vibrational response at 1,740 cm^{-1} using AFM-IR (Fig. 3), indicating saturated ester C=O stretches. The response at 1,640 cm^{-1} was found in a vessel-parenchyma pit membrane and developing cell wall, showing the presence of amide I (C=O stretch), but was not found in an intervessel pit membrane and secondary wall (Fig. 3). In addition, there was a signal in all fingerprints of carbonyl (1,810–1,640 cm^{-1}) and alkenes (1,660–1,600 cm^{-1}), which can mean several compounds, including phospholipids, cholesterol esters, hemicellulose, pectin, lignin, and proteins. The chemical maps show the spatial distribution of the 1,740 cm^{-1} (Fig. 4, B and E) and 1,640 cm^{-1} (Fig. 4, C, F, and I) peaks, considering that only these peaks presented signal in the single-point spectra (Fig. 3).

DISCUSSION

Debates about the chemical composition of pit membranes in several angiosperm species have been contradictory, at least partly due to the indirect or low-resolution methods used (Bamber, 1961; Bauch and Berndt, 1973; Sano and Fukuzawa, 1994; Fineran, 1997; Donaldson, 2001; Fromm et al., 2003; Boyce et al., 2004; Schmitz et al., 2008; Herbette et al., 2015; Klepsch et al., 2016; Schenk et al., 2017). We show here that IR nanospectroscopy can be applied to study plant cell walls at a nanoscale, allowing us to study the heterogeneity of their chemical composition.

Table 1. Summary of all characteristic IR peaks shown in Figure 2, with reference to the cell wall compounds based on the literature (Kumar et al., 2016; Türker-Kaya and Huck, 2017), and potential differences between different cell wall structures

When most scans (Fig. 2, thin blue lines) showed convergent peaks, the signal was interpreted to be strong (S). Otherwise, when the signal is near zero (arbitrary unit) or with less convergent peaks and/or nearby peaks, the spectral peaks were classified as providing a weak signal (W).

Characteristic Peak cm^{-1}	Assignment	Compound	Cell Wall Structure		
			Vessel-Vessel Pit Membrane	Vessel-Parenchyma Pit Membrane	Developing Cell Wall
1,510	C=C aromatic stretch	Lignin	S	W	W
1,625	C=C stretch	Phenolic	S	W	W
1,145	C-O-C asymmetric stretch	Cellulose	S	S	W
1,205	O-H in plane bend	Cellulose	S	S	W
1,075	C-O ring stretch	Pectin	W	S	S
1,460	Amide III (aromatic hydrocarbons)	Protein	no	S	S
1,550	Amide II (C=N and N-H stretch)	Protein	W	S	S

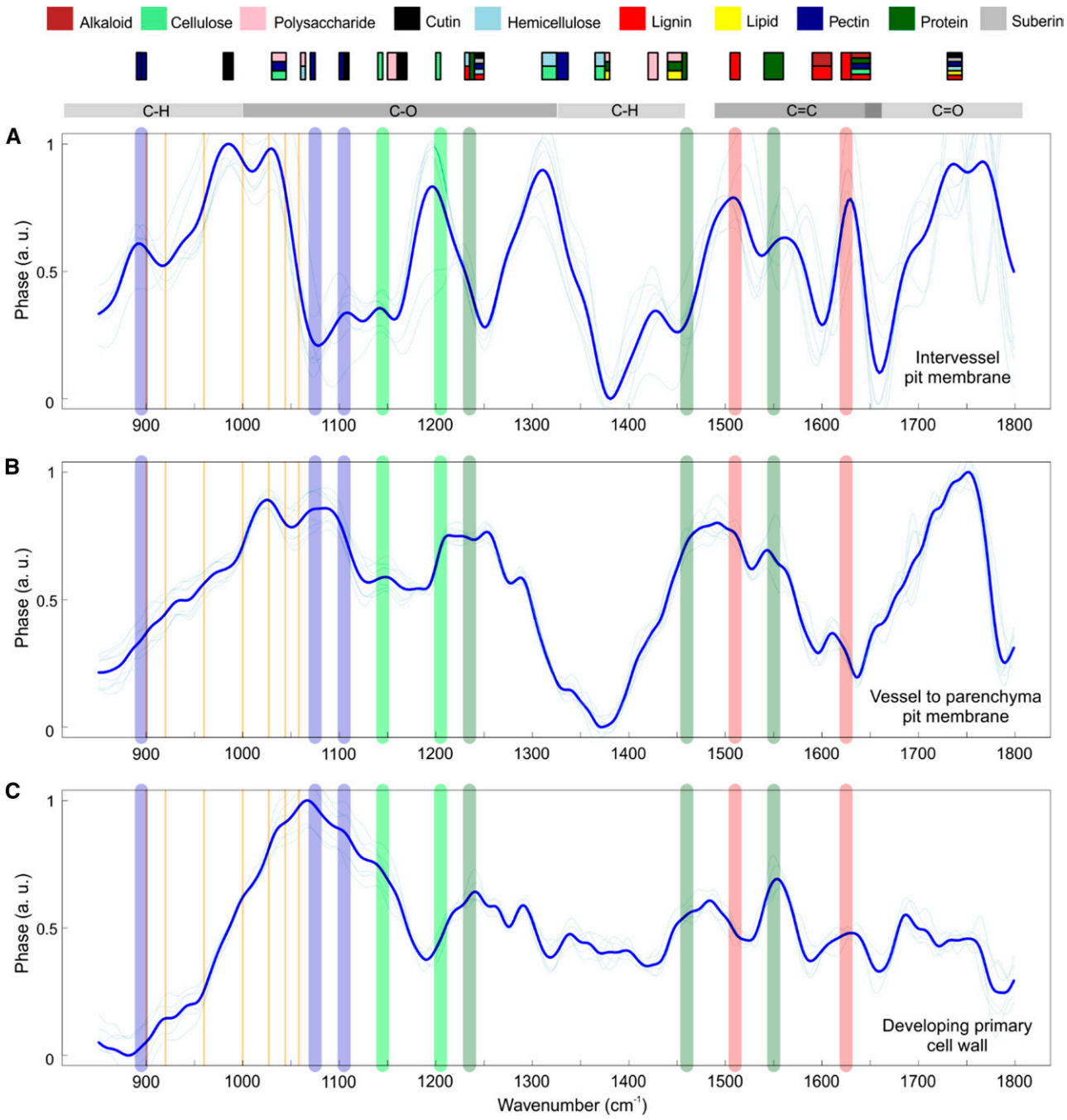

Figure 2. SINS spectra of *P. nigra* wood. A, Intervessel pit membrane. B, Vessel to parenchyma pit membrane. C, Developing primary cell wall. The thin blue lines are individual spectra (based on at least 10 scans at each point), and the thick blue lines are the spectra averages of all measurements for that structure. Boxes on the top mark regions where peaks of specific substances occur (see color legend). Thick vertical lines mark peaks unique for one specific substance. Vertical orange lines mark regions where sample contamination may have occurred. a.u., arbitrary unit.

The SINS spectra (Fig. 2; Supplemental Fig. S1), partially supported by the AFM-IR results (Figs. 3 and 4), showed various carbon bond types in the C-H, C-O, C=C, and C=O regions, indicating a more complex chemical composition of the pit membrane than previously thought. Cellulose and phenolic compounds occur in intervessel pit membranes of *P. nigra* with a lower signal for proteins (Table 1). In the developing cell wall and vessel-parenchyma pit membrane of *P. nigra*, there was a stronger signal of protein and a weaker signal of phenolic compounds than in the intervessel pit membrane. The AFM-IR spectra partially

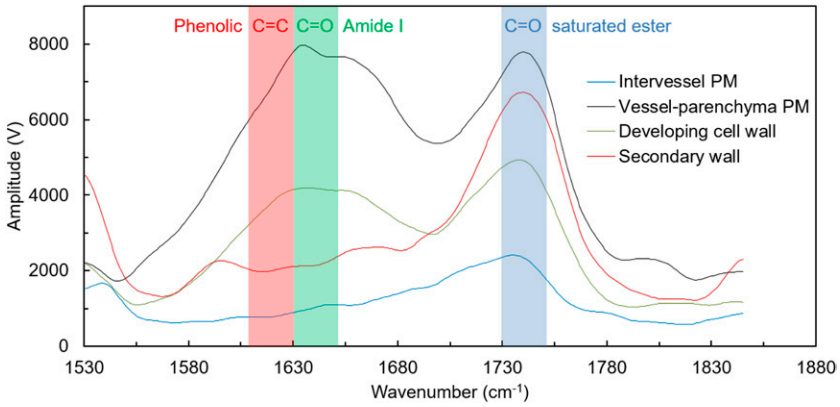

Figure 3. AFM-IR spectra of *P. nigra* wood. Each spectrum is an average of 256 accumulations from the intervessel pit membrane (PM; blue line), vessel-parenchyma pit membrane (black line), developing cell wall (green line), and secondary cell wall (red line).

corroborate the SINS spectra results in the range from 1,530 to 1,845 cm^{-1} (the laser tuning range of the AFM-IR device used; Fig. 3), although the 1,625 cm^{-1} peak was not present in the intervessel pit membrane spectra. The AFM-IR signal scales with the number and strength of the molecular functional group oscillating under the laser-illuminated confocal volume (Lu et al., 2014). Thus, it is possible that the intervessel pit membranes measured, typically up to 30 nm (data not shown), were too thin for us to obtain a reasonable AFM-IR signal-to-noise ratio. In fact, the AFM-IR spectra of this structure showed the weaker spectrum among the set (Fig. 3).

The AFM-IR chemical map that highlights the 1,740 cm^{-1} peak is robust for cell walls (including the pit membrane and developing cell wall; Fig. 4, B, E, and I), but it provides a lower signal for cytoplasmic contents than the 1,640 cm^{-1} peak (amide I; Fig. 4, C and F). Thus, as the 1,740 cm^{-1} peak represents a saturated ester C=O stretch, this strong signal would be related to compounds that are always found in cell walls, such as hemicellulose, pectin, and lignin, and a lower signal from compounds abundant in cell organelles, such as phospholipid and cholesterol esters. The 1,640 cm^{-1} peak is absent in the intervessel pit membrane and secondary wall using AFM-IR (Fig. 3). Therefore, it is likely that the C=O stretch signals indicate proteins and not other possible compounds (phenolic compounds, pectin, cellulose, or alkaloids) in the vessel-parenchyma pit membrane and developing cell wall.

It is important to note that the spectral stability in the SINS and AFM-IR experiments depends strongly on the complexity of the chemistry of the sample. The thermal drifts of the AFM piezoelectric stages were usually about 100 nm per hour. Thus, if a sample is chemically heterogeneous inside a 100- × 100-nm area, which is a typical AFM footprint for a 20- to 30-min point spectrum, the spectrum will be a chemical average of all material phases inside that area. Moreover, nanospectra at a 25-nm spatial resolution and from less than 100-nm-thick layers represent the scattering of only a few thousands chemical bonds. These factors can explain the variance observed in the shape and intensity of the spectra analyzed. Despite possible interfering factors, we had high convergence in the peaks that reflect plant compounds, which indicates that most signals measured are robust and above the noise level.

There is a general consensus that cellulose is present in intervessel pit membranes (Herbette et al., 2015; Klepsch et al., 2016), as confirmed in our results (O-H and C-O-C vibrations at 1,205 and 1,145 cm^{-1}), which also was shown for vessel-parenchyma pit membranes. There was a weak signal for cellulose only in the developing primary wall. We also found shared peaks for cellulose and other cell wall polysaccharides such as hemicellulose (peaks 1,320 and 1,235 cm^{-1}). While the hydrolysis of the cell wall possibly removes all hemicellulose from the intervessel pit membrane (O'Brien, 1970; Kim and Daniel, 2013; Herbette et al., 2015; Klepsch et al., 2016), our results do not provide any additional information about the occurrence of hemicellulose in the pit membrane because there is no unique peak in the IR spectra for this compound.

The presence of phenolic compounds in the intervessel pit membrane was shown using SINS by the characteristic peaks at 1,510 and 1,625 cm^{-1}. This result is in line with several observations using different techniques (Fromm et al., 2003; Boyce et al., 2004; Schmitz et al., 2008, 2012; Herbette et al., 2015). There was a lower signal in vessel-parenchyma pit membranes and developing cell walls than in intervessel pit membranes. A signal next to 1,530 cm^{-1} (C=C vibration) also was found using AFM-IR in all structures (Fig. 3). The 1,510 cm^{-1} peak, which is out of the bandwidth covered by the AFM-IR device that we used in this study, is characteristic of lignin (Karunakaran et al., 2015; Kumar et al., 2016; Türker-Kaya and Huck, 2017), but the C=C aromatic stretch also could be found in free monolignols, ferulic acid, and other phenolic

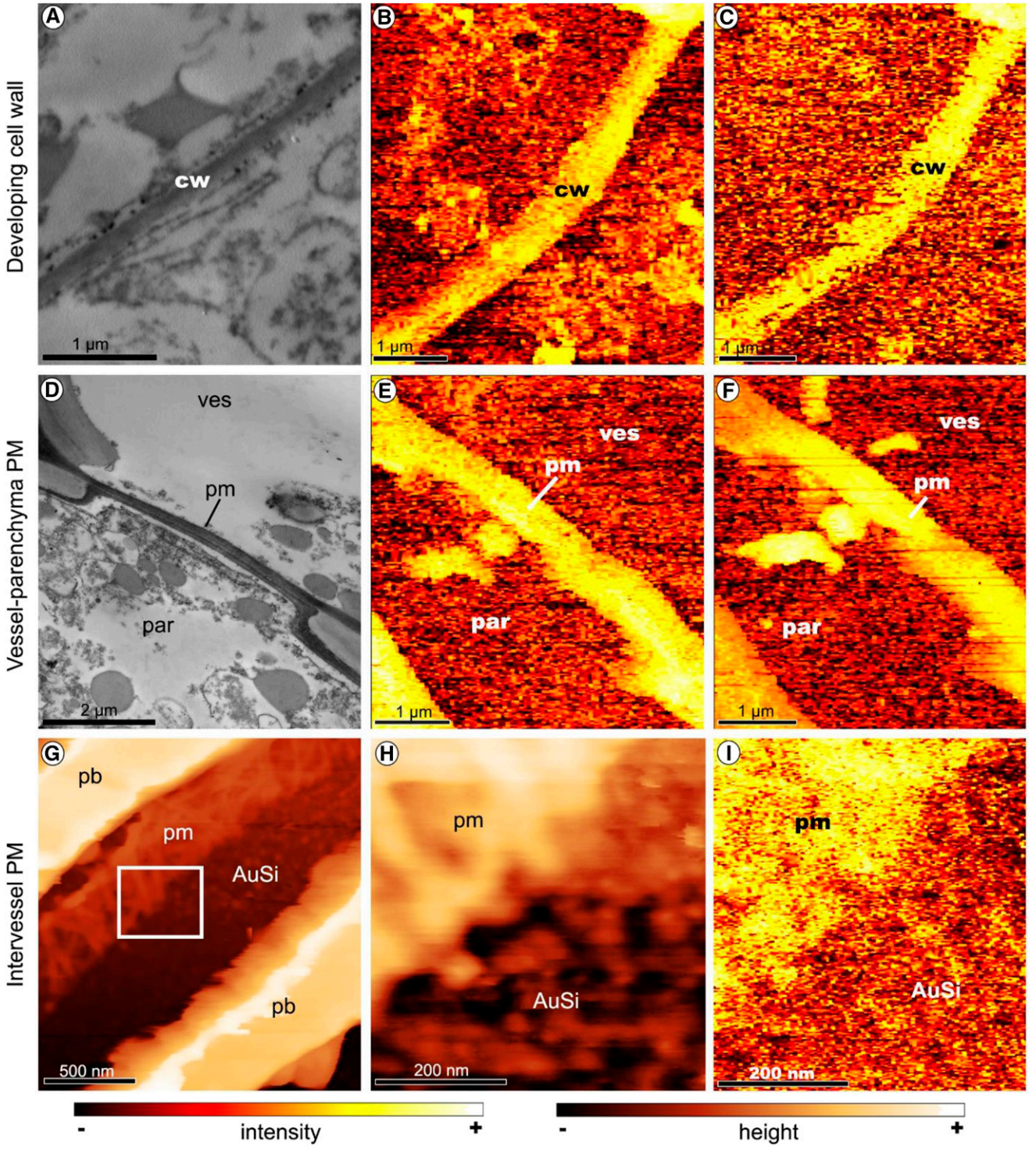

Figure 4. Transmission electron microscopy and AFM-IR chemical mapping images of *P. nigra* wood. Transmission electron microscopy images (A and D) show similar structures to the corresponding chemical mapping (B-C and E-F, respectively) at the characteristic peaks found in each structure, 1,740 cm^{-1} (B and E) and 1,640 cm^{-1} (C, F, and I), based on AFM-IR. G and H are AFM height images of intervessel pit membranes. The white box in G and images H and I correspond to the same area. AuSi, AuSi plate; cw, cell wall; par, parenchyma; pb, pit border; pm, pit membrane; ves, vessel.

compounds. Most of these compounds can be oxidized and incorporated into cell wall polymers (de O Buanafina, 2009; Vanholme et al., 2010). Although we used healthy plants in our study, we cannot ignore the possibility that phenolic compounds were introduced by pathogens into the xylem sap and these phenolics were then detected in our analyses (Wallis and Chen, 2012). If phenolics were incorporated in the cell wall polymers or deposited onto the pit membrane, these compounds should change their surface properties. The presence and proportion of phenolics, including monolignols, also might change the wettability of the intervessel pit membrane and, consequently, would reduce the capillary pressure developed in the air-to-water interface, decreasing the resistance to embolism (Herbette et al., 2015; Pereira et al., 2018). The wettability of the pit membrane also would be affected by the presence of amphiphilic lipids in xylem sap, which function as surfactants. Recently, Schenk et al. (2018) found surfactants covering cell wall surfaces, and their presence on or in the pit membrane may encapsulate the air bubbles that cross its nanopores, keeping bubbles stable and preventing them from expansion and forming an embolism (Jansen and Schenk, 2015; Schenk et al., 2015, 2017). The presence of lignin also may provide mechanical resistance to pit membranes, which is needed to maintain their integrity under negative pressures, because any fracture or considerable stretching may result in pit membrane shrinkage and increased vulnerability to embolism (Hacke et al., 2001; Tixier et al., 2014; Hillabrand et al., 2016; Zhang et al., 2017). On the other hand, lignin as well as pectin have higher electric potentials than cellulose, which, depending on the sap ionic composition, should result in high electroviscosity and change the hydraulic conductivity efficiency (Santiago et al., 2013).

There was a clear signal of pectin (1,105 and 1,075 cm^{-1}) in the vessel-parenchyma pit membrane and developing cell wall. Pectin occurs in the amorphous layer of vessel-parenchyma pit membranes (Rioux et al., 1998; Kim and Daniel, 2013; Herbette et al., 2015; Klepsch et al., 2016) and also may occur in the actual pit membrane, although hydrolytic enzymes are suggested to remove all noncellulosic compounds in the actual pit membrane (Kim and Daniel, 2013; Herbette et al., 2015). McCann et al. (1992) showed that the 1,740 cm^{-1} peak disappeared when pectin was extracted from cell walls of onion (*Allium cepa*), although, in that case, there was no signal of phenolic compounds. This 1,740 cm^{-1} peak is related to C=O stretches and also may be attributed to phenolic compounds, which was found in our spectra. Despite the presence of signals at 1,105 and 1,330 cm^{-1} in the intervessel pit membrane, which would be related to pectin, the peaks near 1,110 and 1,320 cm^{-1} are related to cellulose (Kumar et al., 2016), while the 1,110 cm^{-1} peak also is related to cutin (Türker-Kaya and Huck, 2017). This suggests that either the clear identification of pectin is not attainable, considering the spectral resolution of SINS (6 cm^{-1}), or pectin is not present in the intervessel pit membrane, which is in line with the general lack of pectin in fully developed intervessel pit membranes using different methods (O'Brien and Thimann, 1967; O'Brien, 1970; Klepsch et al., 2016; Schenk et al., 2018). The 895 cm^{-1} peak, also attributed to pectin, can be confounded with possible peaks from dimethyl sulfoxide (DMSO), which was used during the sample preparation (Fig. 2, orange lines).

Several proteins are transported in the xylem sap (Iwai et al., 2003; Buhtz et al., 2004; Gonorazky et al., 2012; Schenk et al., 2017). The amide peaks at 1,550 and 1,460 cm^{-1} were stronger in the vessel-parenchyma pit membrane and developing cell wall than in the intervessel pit membrane. Similar results for the vessel-parenchyma pit membrane and developing cell wall were found using AFM-IR, considering the presence of the 1,640 cm^{-1} peak (amide I) likely due to proteins (Fig. 3). A possible explanation is that living parenchyma cells may produce and secrete proteins that are transported over the amorphous layer and the pit membrane of vessel-parenchyma pits. These proteins also could be involved in the so-called black cap on the outermost layer of the pit membrane facing the vessel lumen (Schenk et al., 2017).

There are few reports about plant cell wall chemistry at the nanoscale without using any form of extraction or special treatment. The techniques used in these studies are based on IR spectroscopy, either using AFM-IR (Wang et al., 2016) or an analogous technique, such as photonic-nanomechanical force microscopy (Tetard et al., 2015; Farahi et al., 2017). Wang et al. (2016) accurately measured the penetration of resin in the cell wall using AFM-IR. Tetard et al. (2015) and Farahi et al. (2017) also identified nanoscale compositional changes of lignin and cellulose dominance in the cell wall after treatments with extractives based on photonic-nanomechanical force microscopy. In our case, strong signals from the dominant vibrational resonances are highlighted by narrow-band chemical maps of the pit membrane and surrounding walls using AFM-IR. As an extension, full chemical speciation is provided by the SINS broadband local spectra, which covers most of the typical vibrational resonances found in IR analysis of plant cell structures. However, there were different spectral assignments from different points of the same structure using SINS (Supplemental Fig. S1), which may be related to the sample chemical heterogeneity in the submicron scale and due to the fact that the spectrum should be a chemical average of all phases of the material inside the footprint area, which resulted from the thermal drifts during the measurements. This is an important detail to be considered in further studies. Our study also showed that the preparation of biological samples represents a major bottleneck for SINS, considering the need for sections thinner than 100 nm. However, sample preparation for AFM-IR is easier, since thicker samples can be used (greater than 1 μm; data not shown). As such, future work on AFM-IR with thicker sections would allow testing of the effects of various cryoprotectants and sample preparation

without cryoprotectants. This approach also would be useful to evaluate chemical degradation.

The chemistry of pit membranes seems to be much more complex than previously thought, which may affect the water transport system in plants and especially air seeding mechanisms, considering the presence of hydrophobic compounds. In addition, compounds with a high electric potential, such as lignin and pectin, also could change the xylem hydraulic conductivity due to the electroviscosity effect (Santiago et al., 2013). Further studies could evaluate contrasting hydraulic systems to assess if the pit membrane composition varies among species or plants growing under conditions with different water availability.

MATERIALS AND METHODS

Sample Preparation

We collected the third internodes from branches of *Populus nigra* saplings that were grown in pots in a greenhouse at the University of Campinas. After collection, fresh samples were immediately brought to the laboratory. The internodes were trimmed to expose about 1 mm^2 of the transverse area of vascular tissues and then attached to a cryo-ultramicrotome (Reichert Ultracut FC; Leica Microsystems), which directly froze the samples at −60°C. The temperature of the diamond knife was kept at −80°C. In order to detach frozen sections (about 100 nm in thickness) from the diamond knife, a cryoprotectant solution of DMSO and deionized water (3:2) was required. These sections were then collected and placed on a heated (50°C) AuSi plate, where they were left to dry. It was not possible to transfer the sections to the gold plates when using saturated Suc as an alternative cryoprotectant solution. The plates were stored in vacuum chambers until the SINS and AFM-IR measurements were performed.

Treatment of the xylem with hot water and overnight incubation in DMSO can be used to extract cell wall polysaccharides, especially hemicellulose in primary cell walls (Catesson, 1989). Although we exposed the sample to DMSO for a few minutes until it was completely dry at 50°C on an AuSi plate, the cell walls did not show degradation in the AFM or optical images (Supplemental Fig. S2). However, the DMSO may have solubilized a small quantity of polysaccharides and other compounds, which would be diluted in the much higher amount of cryoprotectant and, thus, decreased the IR signal in our spectra. Despite the potential for contamination by DMSO, it was not possible to prepare ultrathin sections without applying the cryoprotectant. One may argue that, due to the large quantity of DMSO that was used, any potential extractives are likely diluted, which may not result in false positives at various parts of the cell wall.

It was important to work with ultrathin sections for SINS measurements. Since the penetration depth of the technique is typically 50 to 150 nm, measuring thin sample slices mounted on Au allowed the SINS signal to be enhanced via interaction with the metallic surface underneath. Most s-SNOM studies on organic systems probe samples that are a few tens of nanometers thick (typically less than 100 nm; Taubner et al., 2004; Atkin et al., 2012; Huth et al., 2012; Amenabar et al., 2013; Govyadinov et al., 2013; Pollard et al., 2014, 2016). Despite the recent discussion about the role of sample thickness in the s-SNOM analysis of polymers (Mastel et al., 2015), we decided to focus on producing sections no thicker than 100 nm. In previous tests with samples that were fixed and embedded in LR White resin according to standard methods, such as for transmission electron microscopy, it was not possible to distinguish the cell wall from the resin spectra (data not shown). Resins can almost entirely penetrate the cell wall and can be detected in IR spectra (Wang et al., 2016). Considering the challenging sample preparation procedure without any fixative and resin, only a few cuts of one sample from *P. nigra* were sufficiently thin and flat enough for SINS and AFM-IR measurements. However, the chemical heterogeneity was studied at the nanoscale for at least three intervessel pit membranes, three vessel-parenchyma pit membranes, and three developing primary cell walls. At least three different regions of each structure were investigated. Moreover, each structure was scanned between 50 and 120 times (see next section).

Considering that the samples were prepared without any fixative and only conserved in a dry atmosphere, it is possible that some compounds might have undergone chemical changes before the measurements. The dehydration of the sample for transmission electron microscopy, using propanol and ethanol, can strongly affect compounds such as lipids and phospholipids (Schenk et al., 2018). It is likely that apoplastic lipids associated with pit membranes have undergone changes. Moreover, we cannot evaluate the effect of dehydration on lipids or phospholipids in our samples, since there is no characteristic IR peak from these compounds.

The same internodes also were used to identify the tissues and cell types using transmission electron microscopy. For this, the samples were fixed in 2.5% (v/v) glutaraldehyde in 0.1 M sodium cacodylate buffer at pH 7.4 for 12 h and then postfixed with 1% osmium tetroxide aqueous solution in the dark for 12 h. Dehydration was achieved by ascending in an alcohol series from 10% to 100%. After dehydration, the material was included in hydrophilic acrylic resin LR White Medium Grade (EMS). Samples were included in gelatin capsules and left to polymerize at 60°C for 12 h. Ultrathin sections were made with an ultramicrotome (Ultracut UCT; Leica Microsystems) using a diamond knife (Drukker; 60 nm thick). Poststaining was performed using an aqueous solution of 2% uranyl acetate and a lead solution for 30 min each. The observations were performed with a transmission electron microscope (LEO 906; Carl Zeiss).

The SINS and AFM-IR measurements were made for the following three structures in *P. nigra*: (1) developing primary radial walls from cells of the cambial zone (Supplemental Fig. S3, A and B); (2) vessel-parenchyma pit membranes (Supplemental Fig. S3, C and D); and (3) intervessel pit membranes (Supplemental Fig. S3, E–G). The secondary wall of the pit border (Supplemental Fig. S3G) also was measured using AFM-IR, but considering the thickness of secondary wall regions, it was not possible to measure this structure using SINS. However, we could not identify whether all intervessel pit membranes actually occurred between adjacent vessels or whether vessel-tracheid or tracheid-tracheid pit membranes were included. However, these pit membrane types are similar in morphology and function (Sano et al., 2011).

SINS and AFM-IR Measurements

SINS measurements took place at the IR-Nanospectroscopy Endstation (IR1) of the Brazilian Synchrotron Light Laboratory (LNLS), a beamline that collects both continuous and edge IR radiation from a 1.67-T dipole in a 1.37-GeV synchrotron accelerator (Moreno et al., 2013; Freitas et al., 2018). The LNLS accelerator runs experiments in shifts of 12 h in decay mode (i.e. the IR intensity is proportional to the stored current from 250 mA [beginning of the shift] to 100 mA [end of the shift]). The SINS experimental station is equipped with a commercially available s-SNOM instrument (NeaSNOM; Neaspec) that is able to couple the IR synchrotron beam to the AFM device. Platinum-coated silicon AFM tips (PtIr Arrow; NanoWorld) were used for subdiffractional light confinement. Due to the special interferometric arrangement of s-SNOM, which uses asymmetric Michelson interferometry, both the amplitude and phase of the scattered signal can be detected. For material with weak oscillators, such as organics, both the phase and the imaginary spectrum of s-SNOM carry absorption properties of the sample (Huth et al., 2012; Govyadinov et al., 2013). All SINS data were acquired using lock-in detection on higher-harmonics demodulation (Keilmann and Hillenbrand, 2004; second harmonic) of the tip resonance frequency (~300 kHz). Both topography and SINS were performed using tapping mode AFM. SINS can conceptually generate chemical maps via hyperspectral imaging, which consists of taking an array or map of a point spectrum. By Fourier processing the data, it is possible to reconstruct a chemical image taking specific slices of energy. However, due to the long acquisition times required of this imaging modality, this analysis is only feasible for the study of materials with a strong vibrational response (e.g. polar crystalline materials with strong phonon activity; Freitas et al., 2018). For this reason, the nanospectroscopy was taken from a single point (resolution of 25 nm) on different cell wall structures, which were acquired using 6 cm^{-1} spectral resolution covering the spectral range from 700 to 1,800 cm^{-1}. The simultaneous AFM images generated by SINS were used as a morphological guide for the definition of areas of interest. Each spectrum is an average of at least 10 scans composed of 2,048 points with an integration time of 19.3 ms at each point. All SINS data were measured under a dry and thermally controlled environment (relative humidity less than 3% and temperature variation less than 0.1°C h^{-1}) to prevent IR absorption by water and thermal drifts of the AFM piezoelectric stages. The thermal drift was evaluated by sequential AFM images taken in the same position. When drift occurred, usually about 100 nm per hour, we

reduced the number of scans to ensure that the spectrum was taken at the same location. In this case, we increased the number of measurements, resulting in 50 to 120 scans for each structure.

AFM-IR experiments were performed using the nanoIR2 AFM-IR instrument (Anasys Instruments) installed in the Laboratory for Surface Science of the Brazilian Nanotechnology National Laboratory. A pulsed Quantum Cascade Laser (MIRcat QCL from Daylight Solutions) covered a spectral range from 1,530 to 1,845 cm^{-1}. Narrow-band AFM-IR chemical images were recorded with 1 cm^{-1} spectral resolution. Both topography and AFM-IR images were acquired using Au-coated Si AFM cantilevers (ContGB-G; Budget Sensors) working in contact mode AFM. During the acquisition of AFM-IR maps, no thermal damage was noticed.

Data Analysis

For all samples, we adopted the phase spectra as a direct measurement of the IR absorbance, a standard procedure in s-SNOM molecular analysis (Huth et al., 2012; Govyadinov et al., 2013). To correct the decay mode of the synchrotron storage ring, we divided each phase spectrum by the instant stored current for standardizing the IR intensity. Frequencies lower than 850 cm^{-1} and higher than 1,800 cm^{-1} were not used in the analysis, as they showed low signals in our experimental setup (Supplemental Fig. S4). We applied a moving window average filter over 10-point intervals in all spectra to filter high-frequency noise (filter function in R; Supplemental Fig. S5). Phase correction (phase tilt correction) was performed by baseline subtraction of linear regression fitting of each spectrum and by using its residuals as the corrected phase data. Finally, we plotted the spectra of each cell structure (thick blue lines in Fig. 2) as an average of the set of individual spectra at each frequency in that structure (thin blue lines in Fig. 2). We verified the presence or absence of peaks manually in the mean spectra of a structure. If a peak was relatively weak, we analyzed the set of individual spectra (thin blue lines in Fig. 2) to check whether there was consistency in that particular average peak with respect to the individual spectra. In other words, in our analyses, double checking the set of peaks that compose an average peak eliminated the peaks produced by random noise. When most individual spectra showed convergent peaks, the signal was interpreted to be strong. Otherwise, when the signal is near zero (arbitrary unit) or with less convergent peaks and/or nearby peaks, the spectral peaks were classified as providing a weak signal. We used a previous characterization of a plant cell analyzed by IR techniques (Kumar et al., 2016; Türker-Kaya and Huck, 2017) to associate peaks with chemical bonds and chemical compounds (see list in Supplemental Table S1). All data were processed in the programming environment R with base statistical packages (R Core Team, 2013).

Supplemental Data

The following supplemental materials are available.

Supplemental Figure S1. SINS spectra of all structures analyzed.

Supplemental Figure S2. General aspect of the sample used for the measurements by light and atomic force microscopes.

Supplemental Figure S3. Transmission electron microscopy of the developing primary radial wall, vessel-parenchyma pit membrane, and intervessel pit membrane of *P. nigra*.

Supplemental Figure S4. Nonstandardized IR amplitude spectra of a reference gold plate.

Supplemental Figure S5. An example of IR phase spectra processing for a *P. nigra* vessel to a vessel pit membrane.

Supplemental Table S1. Peak assignment considered in data analysis.

ACKNOWLEDGMENTS

We thank the LNLS for providing beamtime at the IR1 beamline, and especially Thiago M. dos Santos, Francisco Maia, and Neaspec for technical support during the SINS experiment. We also thank the team from the Laboratory for Surface Science of the Brazilian Nanotechnology National Laboratory, Evandro Lanzoni, Carlos Costa, and Christoph Deneke, for providing access and technical support with the AFM-IR measurements, and Lidiane C. Costa from UFSCar for sample preparation using cryo-ultramicrotomy.

Received February 5, 2018; accepted May 24, 2018; published June 5, 2018.

LITERATURE CITED

Amarie S, Zaslansky P, Kajihara Y, Griesshaber E, Schmahl WW, Keilmann F (2012) Nano-FTIR chemical mapping of minerals in biological materials. Beilstein J Nanotechnol **3**: 312–323

Amenabar I, Poly S, Nuansing W, Hubrich EH, Govyadinov AA, Huth F, Krutokhvostov R, Zhang L, Knez M, Heberle J, (2013) Structural analysis and mapping of individual protein complexes by infrared nanospectroscopy. Nat Commun **4**: 2890

Atkin JM, Berweger S, Jones AC, Raschke MB (2012) Nano-optical imaging and spectroscopy of order, phases, and domains in complex solids. Adv Phys **61**: 745–842

Bamber RK (1961) Staining reaction of the pit membrane of wood cells. Nature **4786**: 409–410

Bauch J, Berndt H (1973) Variability of the chemical composition of pit membranes in bordered pits of gymnosperms. Wood Sci Technol **7**: 6–19

Bechtel HA, Muller EA, Olmon RL, Martin MC, Raschke MB (2014) Ultrabroadband infrared nanospectroscopic imaging. Proc Natl Acad Sci USA **111**: 7191–7196

Boyce CK, Zwieniecki MA, Cody GD, Jacobsen C, Wirick S, Knoll AH, Holbrook NM (2004) Evolution of xylem lignification and hydrogel transport regulation. Proc Natl Acad Sci USA **101**: 17555–17558

Buhtz A, Kolasa A, Arlt K, Walz C, Kehr J (2004) Xylem sap protein composition is conserved among different plant species. Planta **219**: 610–618

Catesson AM (1989) Specific characters of vessel primary walls during the early stages of wood differentiation. Biol Cell **67**: 221–226

Choat B, Cobb AR, Jansen S (2008) Structure and function of bordered pits: new discoveries and impacts on whole-plant hydraulic function. New Phytol **177**: 608–625

Dazzi A, Prazeres R, Glotin F, Ortega JM (2005) Local infrared microspectroscopy with subwavelength spatial resolution with an atomic force microscope tip used as a photothermal sensor. Opt Lett **30**: 2388–2390

Dazzi A, Prazeres R, Glotin F, Ortega JM (2006) Subwavelength infrared spectromicroscopy using an AFM as a local absorption sensor. Infrared Phys Technol **49**: 113–121

Dazzi A, Glotin F, Carminati R (2010) Theory of infrared nanospectroscopy by photothermal induced resonance. J Appl Phys **107**: 124519

de O Buanafina MM (2009) Feruloylation in grasses: current and future perspectives. Mol Plant **2**: 861–872

Donaldson LA (2001) Lignification and lignin topochemistry: an ultrastructural view. Phytochemistry **57**: 859–873

Farahi RH, Charrier AM, Tolbert A, Lereu AL, Ragauskas A, Davison BH, Passian A (2017) Plasticity, elasticity, and adhesion energy of plant cell walls: nanometrology of lignin loss using atomic force microscopy. Sci Rep **7**: 152

Fineran BA (1997) Cyto- and histochemical demonstration of lignins in plant cell walls: an evaluation of the chlorine water/ethanolamine-silver nitrate method of Coppick and Fowler. Protoplasma **198**: 186–201

Freitas RO, Deneke C, Maia FCB, Medeiros HG, Moreno T, Dumas P, Petroff Y, Westfahl H (2018) Low-aberration beamline optics for synchrotron infrared nanospectroscopy. Opt Express **26**: 11238–11249

Fromm J, Rockel B, Lautner S, Windeisen E, Wanner G (2003) Lignin distribution in wood cell walls determined by TEM and backscattered SEM techniques. J Struct Biol **143**: 77–84

Gonorazky G, Laxalt AM, Dekker HL, Rep M, Munnik T, Testerink C, de la Canal L (2012) Phosphatidylinositol 4-phosphate is associated to extracellular lipoproteic fractions and is detected in tomato apoplastic fluids. Plant Biol (Stuttg) **14**: 41–49

Govyadinov AA, Amenabar I, Huth F, Carney PS, Hillenbrand R (2013) Quantitative measurement of local infrared absorption and dielectric function with tip-enhanced near-field microscopy. J Phys Chem Lett **4**: 1526–1531

Hacke UG, Stiller V, Sperry JS, Pittermann J, McCulloh KA (2001) Cavitation fatigue: embolism and refilling cycles can weaken the cavitation resistance of xylem. Plant Physiol **125**: 779–786

Herbette S, Bouchet B, Brunel N, Bonnin E, Cochard H, Guillon F (2015) Immunolabelling of intervessel pits for polysaccharides and lignin helps in understanding their hydraulic properties in Populus tremula × alba. Ann Bot **115**: 187–199

Hermann P, Hoehl A, Patoka P, Huth F, Rühl E, Ulm G (2013) Near-field imaging and nano-Fourier-transform infrared spectroscopy using broadband synchrotron radiation. Opt Express **21**: 2913–2919

Hillabrand RM, Hacke UG, Lieffers VJ (2016) Drought-induced xylem pit membrane damage in aspen and balsam poplar. Plant Cell Environ **39**: 2210–2220

Huber AJ, Ziegler A, Köck T, Hillenbrand R (2009) Infrared nanoscopy of strained semiconductors. Nat Nanotechnol **4**: 153–157

Huber AJ, Wittborn J, Hillenbrand R (2010) Infrared spectroscopic near-field mapping of single nanotransistors. Nanotechnology **21**: 235702

Huth F, Govyadinov A, Amarie S, Nuansing W, Keilmann F, Hillenbrand R (2012) Nano-FTIR absorption spectroscopy of molecular fingerprints at 20 nm spatial resolution. Nano Lett **12**: 3973–3978

Iwai H, Usui M, Hoshino H, Kamada H, Matsunaga T, Kakegawa K, Ishii T, Satoh S (2003) Analysis of sugars in squash xylem sap. Plant Cell Physiol **44**: 582–587

Jansen S, Schenk HJ (2015) On the ascent of sap in the presence of bubbles. Am J Bot **102**: 1561–1563

Jansen S, Choat B, Pletsers A (2009) Morphological variation of intervessel pit membranes and implications to xylem function in angiosperms. Am J Bot **96**: 409–419

Karunakaran C, Christensen CR, Gaillard C, Lahlali R, Blair LM, Perumal V, Miller SS, Hitchcock AP (2015) Introduction of soft x-ray spectromicroscopy as an advanced technique for plant biopolymers research. PLoS ONE **10**: e0122959

Kawata S, Inouye Y (1995) Scanning probe optical microscopy using a metallic probe tip. Ultramicroscopy **57**: 313–317

Keilmann F, Hillenbrand R (2004) Near-field microscopy by elastic light scattering from a tip. Philos Trans A Math Phys Eng Sci **362**: 787–805

Kim JS, Daniel G (2013) Developmental localization of homogalacturonan and xyloglucan epitopes in pit membranes varies between pit types in two poplar species. IAWA J **34**: 245–262

Klepsch MM, Schmitt M, Knox JP, Jansen S (2016) The chemical identity of intervessel pit membranes in Acer challenges hydrogel control of xylem hydraulic conductivity. AoB Plants **8**: plw052

Knoll B, Keilmann F (1999) Near-field probing of vibrational absorption for chemical microscopy. Nature **399**: 134–137

Kumar S, Lahlali R, Liu X, Karunakaran C (2016) Infrared spectroscopy combined with imaging: a new developing analytical tool in health and plant science. Appl Spectrosc Rev **51**: 466–483

Li S, Klepsch M, Jansen S, Schmitt M, Lens F, Karimi Z, Schuldt B, Espino S, Schenk HJ (2016) Intervessel pit membrane thickness as a key determinant of embolism resistance in angiosperm xylem. IAWA J **37**: 152–171

Lu F, Jin M, Belkin MA (2014) Tip-enhanced infrared nanospectroscopy via molecular expansion force detection. Nat Photonics **8**: 307–312

Mastel S, Govyadinov AA, De Oliveira TVAG, Amenabar I, Hillenbrand R (2015) Nanoscale-resolved chemical identification of thin organic films using infrared near-field spectroscopy and standard Fourier transform infrared references. Appl Phys Lett **106**: 23113

McCann MC, Hammouri M, Wilson R, Belton P, Roberts K (1992) Fourier transform infrared microspectroscopy is a new way to look at plant cell walls. Plant Physiol **100**: 1940–1947

McCully M, Canny M, Baker A, Miller C (2014) Some properties of the walls of metaxylem vessels of maize roots, including tests of the wettability of their lumenal wall surfaces. Ann Bot **113**: 977–989

Moreno T, Westfahl H, Freitas RDO, Petroff Y, Dumas P (2013) Optical layouts for large infrared beamline opening angles. J Phys Conf Ser **425**: 142003

O'Brien TP (1970) Further observations on hydrolysis of the cell wall in the xylem. Protoplasma **69**: 1–14

O'Brien TP, Thimann KV (1967) Observations on the fine structure of the oat coleoptile. III. Correlated light and electron microscopy of the vascular tissues. Protoplasma **63**: 443–478

Pereira L, Domingues-Junior AP, Jansen S, Choat B, Mazzafera P (2018) Is embolism resistance in plant xylem associated with quantity and characteristics of lignin? Trees (Berl) **32**: 349–358

Pollard B, Muller EA, Hinrichs K, Raschke MB (2014) Vibrational nano-spectroscopic imaging correlating structure with intermolecular coupling and dynamics. Nat Commun **5**: 3587

Pollard B, Maia FCB, Raschke MB, Freitas RO (2016) Infrared vibrational nanospectroscopy by self-referenced interferometry. Nano Lett **16**: 55–61

R Core Team (2013) R: A Language and Environment for Statistical Computing. R Foundation for Statistical Computing, Vienna

Rioux D, Nicole M, Simard M, Ouellette GB (1998) Immunocytochemical evidence that secretion of pectin occurs during gel (gum) and tylosis formation in trees. Phytopathology **88**: 494–505

Sano Y, Fukuzawa K (1994) Structural variations and secondary changes in pit membranes in *Fraxinus mandshurica* var. japonica. IAWA J **15**: 283–291

Sano Y, Morris H, Shimada H, Ronse De Craene LP, Jansen S (2011) Anatomical features associated with water transport in imperforate tracheary elements of vessel-bearing angiosperms. Ann Bot **107**: 953–964

Santiago M, Pagay V, Stroock AD (2013) Impact of electroviscosity on the hydraulic conductance of the bordered pit membrane: a theoretical investigation. Plant Physiol **163**: 999–1011

Schenk HJ, Steppe K, Jansen S (2015) Nanobubbles: a new paradigm for air-seeding in xylem. Trends Plant Sci **20**: 199–205

Schenk HJ, Espino S, Romo DM, Nima N, Do AYT, Michaud JM, Papahadjopoulos-Sternberg B, Yang J, Zuo YY, Steppe K, (2017) Xylem surfactants introduce a new element to the cohesion-tension theory. Plant Physiol **173**: 1177–1196

Schenk HJ, Espino S, Rich-Cavazos SM, Jansen S (2018) From the sap's perspective: the nature of vessel surfaces in angiosperm xylem. Am J Bot **105**: 172–185

Schmitz N, Koch G, Schmitt U, Beeckman H, Koedam N (2008) Intervessel pit structure and histochemistry of two mangrove species as revealed by cellular UV microspectrophotometry and electron microscopy: intraspecific variation and functional significance. Microsc Microanal **14**: 387–397

Schmitz N, Koch G, Beeckman H, Koedam N, Robert EMR, Schmitt U (2012) A structural and compositional analysis of intervessel pit membranes in the sapwood of some mangrove woods. IAWA J **33**: 243–256

Sperry JS, Hacke UG, Pittermann J (2006) Size and function in conifer tracheids and angiosperm vessels. Am J Bot **93**: 1490–1500

Sun Q, Greve LC, Labavitch JM (2011) Polysaccharide compositions of intervessel pit membranes contribute to Pierce's disease resistance of grapevines. Plant Physiol **155**: 1976–1987

Sun Q, Sun Y, Walker MA, Labavitch JM (2013) Vascular occlusions in grapevines with Pierce's disease make disease symptom development worse. Plant Physiol **161**: 1529–1541

Sun Q, Sun Y, Juzenas K (2017) Immunogold scanning electron microscopy can reveal the polysaccharide architecture of xylem cell walls. J Exp Bot **68**: 2231–2244

Taubner T, Hillenbrand R, Keilmann F (2004) Nanoscale polymer recognition by spectral signature in scattering infrared near-field microscopy. Appl Phys Lett **85**: 5064–5066

Tetard L, Passian A, Farahi RH, Thundat T, Davison BH (2015) Opto-nanomechanical spectroscopic material characterization. Nat Nanotechnol **10**: 870–877

Tixier A, Herbette S, Jansen S, Capron M, Tordjeman P, Cochard H, Badel E (2014) Modelling the mechanical behaviour of pit membranes in bordered pits with respect to cavitation resistance in angiosperms. Ann Bot **114**: 325–334

Türker-Kaya S, Huck CW (2017) A review of mid-infrared and near-infrared imaging: principles, concepts and applications in plant tissue analysis. Molecules **22**: 168

Vanholme R, Demedts B, Morreel K, Ralph J, Boerjan W (2010) Lignin biosynthesis and structure. Plant Physiol **153**: 895–905

Wallis CM, Chen J (2012) Grapevine phenolic compounds in xylem sap and tissues are significantly altered during infection by *Xylella fastidiosa*. Phytopathology **102**: 816–826

Wang X, Deng Y, Li Y, Kjoller K, Roy A, Wang S (2016) In situ identification of the molecular-scale interactions of phenol-formaldehyde resin and wood cell walls using infrared nanospectroscopy. RSC Adv **6**: 76318–76324

Zenhausern F, Martin Y, Wickramasinghe HK (1995) Scanning interferometric apertureless microscopy: optical imaging at 10 angstrom resolution. Science **269**: 1083–1085

Zhang Y, Klepsch M, Jansen S (2017) Bordered pits in xylem of vesselless angiosperms and their possible misinterpretation as perforation plates. Plant Cell Environ **40**: 2133–2146

Zimmermann MH (1983) Xylem Structure and the Ascent of Sap. Springer-Verlag, Berlin